Electrochimica Acta 54 (2009) 5761–5769

Contents lists available at ScienceDirect

Electrochimica Acta

journal homepage: www.elsevier.com/locate/electacta

Role of hydrophobic anode MPL in controlling water crossover in DMFC

Christian E. Shaffer, Chao-Yang Wang*

Department of Mechanical and Nuclear Engineering, and Electrochemical Engine Center (ECEC), The Pennsylvania State University, 338 Reber Bldg, University Park, PA 16802, United States

ARTICLE INFO

Article history:
Received 20 March 2009
Received in revised form 11 May 2009
Accepted 11 May 2009
Available online 19 May 2009

Keywords:
Direct methanol fuel cell (DMFC)
Highly concentrated fuel
Water management
Anode MPL
Water crossover

ABSTRACT

The importance of reducing water crossover from anode to cathode in a direct methanol fuel cell (DMFC) has been well documented, especially if highly concentrated methanol fuel is to be used. A low-α membrane electrode assembly (MEA) with thin membrane is key to achieving this goal. The low water crossover from anode to cathode for these types of MEAs has traditionally been attributed to the use of a hydrophobic cathode micro-porous layer (MPL). However, it has recently been discovered that a hydrophobic anode MPL also reduces the water crossover, possibly even more significantly than a hydrophobic cathode MPL. In this work, we develop and use a 1D, two-phase transport model that accounts for capillary-induced liquid flow in porous media to explain how a hydrophobic anode MPL controls the water crossover from anode to cathode. We further show that a lower water crossover can lead to a lower methanol crossover via dilution of methanol in the anode catalyst layer. Finally, we perform a parametric study and show that a thicker anode MPL with greater hydrophobicity and lower permeability is more effective in reducing the water crossover.

1. Introduction

In recent years, direct methanol fuel cells (DMFCs) have become a leading contender to replace the lithium-ion (Li-ion) battery as the workhorse power source for mobile devices. Primary reasons for the great attention to DMFC technology include the potential for higher energy density than Li-ion batteries (the theoretical energy density of methanol (MeOH) is ~4800 Wh l^{-1} compared with ~1000–1500 Wh l^{-1} for Li-ion batteries [1]), simple fuel storage, no need for fuel reforming or cell humidification, and simple cell design [2–4]. However, in order to become a viable contender with Li-ion batteries, DMFC designs must first increase their practical energy density in Wh l^{-1}. A key to accomplishing this task is the use of highly concentrated methanol fuel.

The basic half-cell and overall reactions for a DMFC are given by Eq. (1). In the methanol oxidation reaction (MOR), Eq. (1a), 1 mole of H_2O reacts with 1 mole of CH_3OH. In the cathode catalyst layer (cCL), H_2O is produced both via the oxygen reduction reaction (ORR), Eq. (1b), and by crossed-over CH_3OH via the overall reaction, Eq. (1c).

$$CH_3OH + H_2O \rightarrow 6H^+ + 6e^- + CO_2 \quad \text{(anode)} \tag{1a}$$

$$6H^+ + 6e^- + (3/2)O_2 \rightarrow 3H_2O \quad \text{(cathode)} \tag{1b}$$

$$CH_3OH + (3/2)O_2 \rightarrow 2H_2O + CO_2 \quad \text{(overall)} \tag{1c}$$

The fact that H_2O and CH_3OH react stoichiometrically 1:1 in the anode catalyst layer (aCL) is the reason that water management in DMFCs is critically important in order to use high concentration methanol fuel. In order to operate in steady-state, a high concentration methanol fuel cell (HC-MFC) must have a back-flux of water from cathode to anode, as fully elucidated by Wang and co-workers [5–7].

Defining a net water transport coefficient, α, as the net H_2O flux across the membrane (from anode to cathode) normalized by the protonic flux provides a convenient way to characterize the water transport in DMFCs.

$$\alpha = N_{\text{Mem}}^{\text{H}_2\text{O}} \left(\frac{F}{i}\right) \tag{2}$$

Blum et al. [8] proposed a DMFC operating at a water-neutral state, whereby all water needed for the anode MOR is supplied by back-flux from the cathode. In such a design, $\alpha = -1/6$, and theoretically such a cell could operate on neat methanol fuel. Wang and co-workers [5–7] further showed that in order to use even 3 M methanol fuel, a maximum of $\alpha \approx 3$ is allowed; any higher and the cell will run short of water before methanol. This is a startling finding in light of the fact that the 3 M fuel is only roughly 10% methanol by volume, and that it is very common for DMFCs not using low-α MEAs to have $\alpha \approx 3$. The point of low water crossover being critical to the use of highly concentrated MeOH fuel is clearly evident

Abbreviations: DMFC, direct methanol fuel cell; EOD, electro-osmotic drag; HC-MFC, high concentration methanol fuel cell; Li-ion, lithium-ion; MCO, methanol crossover ratio; MEA, membrane electrode assembly; MOR, methanol oxidation reaction; ORR, oxygen reduction reaction.

* Corresponding author. Tel.: +1 814 863 4762; fax: +1 814 863 3491.
E-mail address: cxw31@psu.edu (C.-Y. Wang).

0013-4686/$ – see front matter © 2009 Elsevier Ltd. All rights reserved.
doi:10.1016/j.electacta.2009.05.028

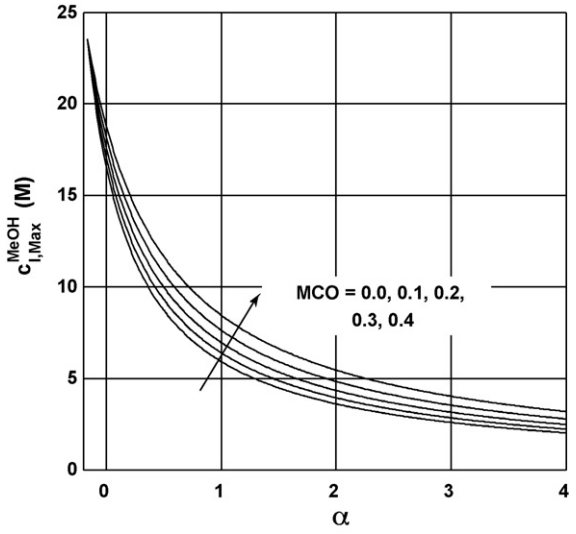

Fig. 1. Maximum methanol fuel concentration vs. net water transport coefficient (α) for steady-state operation.

from Fig. 1, which gives the maximum MeOH fuel concentration as a function of the net water transport coefficient required for steady-state operation. This plot, an extension of the table presented by Liu et al. [6] based on a mass balance analysis on the anode, illustrates that as α becomes smaller, an equivalent reduction in α becomes more effective. This is evident by the steeper slope of the curves as $\alpha \to -1/6$. In this figure, the methanol crossover ratio (MCO) is used to quantify the crossover to the cathode:

$$\mathrm{MCO} = \frac{i_{\mathrm{xover}}}{i + i_{\mathrm{xover}}} = 1 - \eta_{\mathrm{fuel}} \tag{3}$$

Lu et al. [5] and Liu et al. [6] further demonstrated that by using a thin Nafion® 112 membrane along with hydrophobic anode and cathode micro-porous layers (MPLs), they could reduce water crossover to $\alpha \sim 0.6$–0.8 at 60 °C while still maintaining a high fuel efficiency (~80–90%), cell voltage (~0.4 V), and power density (~60 mW cm^{-2}). This type of membrane electrode assembly (MEA) design was first proposed by Lim and Wang [9] and is now commonly referred to as a "low-α MEA". Low-α MEAs have been implemented in various forms by a number of researchers [5–7,9–17].

Within the low-α MEA literature, it has been traditionally believed that a hydrophobic cathode micro-porous layer (cMPL) is the most effective way by which to reduce α via increasing the liquid pressure in the cCL, thereby forcing a back-flow of water to the anode [5–7,9,10,12–15]. However, Liu [16,17] discovered experimentally that a hydrophobic aMPL also plays a significant role in reducing α; using two otherwise identical Nafion® 112-based MEAs with and without hydrophobic aMPL, Liu [16,17] showed $\alpha \sim 0.3$ and $\alpha \sim 1.2$, respectively. Park et al. [11] confirmed this finding by demonstrating a drop in α from ~3.5 to ~1.1 by simply including a hydrophobic aMPL in their Nafion® 1135-based MEA design. It is worth mentioning that many of the conclusions drawn from the modeling results presented in this work are in agreement with the experimental work of Liu [16,17].

The primary purpose of this work is to put forth a theoretical framework of how a hydrophobic anode MPL helps to reduce the water crossover through a low-α MEA with, e.g. thin Nafion® 112 membrane. In doing so we develop and use a 1D, two-phase transport model for the MEA sandwich that accounts for capillary-induced liquid flow in porous media. We further unveil that a lower α can lead to lower methanol crossover due to a dilution effect in the aCL. Finally, through a parametric study we illustrate how a thicker aMPL with greater hydrophobicity and lower permeability can be tailored to further reduce α.

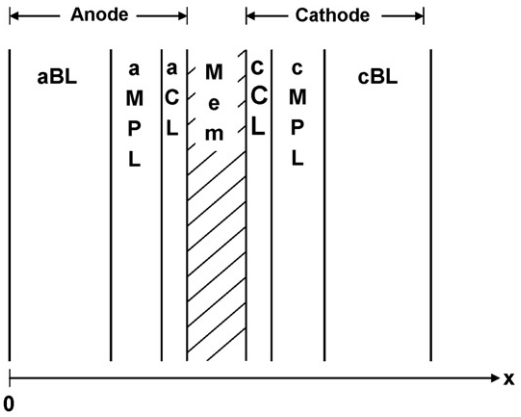

Fig. 2. Geometry of 1D DMFC model.

2. Model

The model presented in the following sections is an extension of a 1D model previously presented by Liu [18]. Major expansions beyond the work [18] include: (1) incorporation of a saturation jump model; (2) incorporation of a cathode mixed potential electrochemistry model; (3) explicit treatment of CLs as zones of finite thickness rather than infinitely thin interfaces; (4) incorporation of an MPL model; (5) the ability to model the transition between a single- and a two-phase region. The addition of the saturation jump model and explicit treatment of the MPLs and CLs are critically important in allowing us to explain the hydrophobic aMPL effect on water crossover, as will be discussed in the sections that follow.

2.1. Basic model setup and assumptions

Fig. 2 gives the geometry of the 1D DMFC model used in this study, showing the distinct regions of the model: anode backing layer (aBL), aMPL, aCL, membrane (Mem), cCL, cMPL, and cathode backing layer (cBL). The model has the following assumptions:

- Steady-state.
- Isothermal.
- In all two-phase regions, there exists thermodynamic equilibrium between the liquid and gas phases.
- Gas-phase pressure assumed uniform over the entire anode and cathode.

2.2. Species fluxes

The total flux of a given species, ψ, is given by the sum of the superficial fluxes in the liquid and vapor phases

$$N^{\psi}(x) = N_l^{\psi}(x) + N_g^{\psi}(x) \tag{4}$$

In a two-phase region on the anode side of the cell, the methanol and H_2O exist in both the liquid and gas phases; however, we assume that the flux of H_2O in the gas phase is negligible due to the equilibrium assumption given in the previous section. In this model, we assume that CO_2 exists only in the gas phase. Assuming a uniform reaction rate in the anode CL, we relate the total species fluxes in the anode regions to the current density by simply utilizing the MOR given by Eq. (1a). The resultant species fluxes are given in Table 1. On the cathode side of the cell, the species fluxes are coupled with the cathode potential based on the detailed reac-

Table 1
Species fluxes for 1D DMFC model.

Region	Species fluxes
aBL, aMPL	$N^{\mathrm{MeOH}}(x) = N^{\mathrm{MeOH}}_{\mathrm{Mem}} + \frac{i}{6F}$; $N^{\mathrm{H_2O}}(x) = N^{\mathrm{H_2O}}_{\mathrm{Mem}} + \frac{i}{6F}$; $N^{\mathrm{CO_2}}(x) = -\frac{i}{6F}$
aCL	$N^{\mathrm{MeOH}}(x) = N^{\mathrm{MeOH}}_{\mathrm{Mem}} + \left(\frac{i}{6F}\right)\left(\frac{x_{\mathrm{aCL/Mem}} - x}{\delta_{\mathrm{aCL}}}\right)$; $N^{\mathrm{H_2O}}(x) = N^{\mathrm{H_2O}}_{\mathrm{Mem}} + \left(\frac{i}{6F}\right)\left(\frac{x_{\mathrm{aCL/Mem}} - x}{\delta_{\mathrm{aCL}}}\right)$; $N^{\mathrm{CO_2}}(x) = \left(-\frac{i}{6F}\right)\left(\frac{x_{\mathrm{aCL/Mem}} - x}{\delta_{\mathrm{aCL}}}\right)$
cCL	$N^{\mathrm{MeOH}}(x) = \begin{cases} N^{\mathrm{MeOH}}_{\mathrm{Mem}} + \left[-\frac{j^{\mathrm{MOR}}_c}{6F} - r_{\mathrm{chem}}\right](x - x_{\mathrm{cCL/Mem}}) & (x_{\mathrm{cCL/Mem}} < x < x^{\mathrm{MeOH}}_o) \\ 0 & (x^{\mathrm{MeOH}}_o < x < x_{\mathrm{cCL/cMPL}}) \end{cases}$
	$N^{\mathrm{H_2O}}(x) = \begin{cases} N^{\mathrm{H_2O}}_{\mathrm{Mem}} + \left[-\frac{j^{\mathrm{MOR}}_c}{6F} + \frac{j^{\mathrm{MOR}}_c}{2F} + 2r_{\mathrm{chem}}\right](x - x_{\mathrm{cCL/Mem}}) + \left[\frac{j^{\mathrm{ORR}} - j^{\mathrm{MOR}}_c}{2F}\right](x - x_{\mathrm{cCL/Mem}}) & (x_{\mathrm{cCL/Mem}} < x < x^{\mathrm{MeOH}}_o) \\ N^{\mathrm{H_2O}}\big|_{x=x^{\mathrm{MeOH}}_o} + \left[\frac{j^{\mathrm{ORR}} - j^{\mathrm{MOR}}_c}{2F}\right](x - x^{\mathrm{MeOH}}_o) & (x^{\mathrm{MeOH}}_o < x < x_{\mathrm{cCL/cMPL}}) \end{cases}$
	$N^{\mathrm{O_2}}(x) = \begin{cases} \left[-\frac{j^{\mathrm{MOR}}_c}{4F} - 1.5r_{\mathrm{chem}}\right](x - x_{\mathrm{cCL/Mem}}) - \left[\frac{j^{\mathrm{ORR}} - j^{\mathrm{MOR}}_c}{4F}\right](x - x_{\mathrm{cCL/Mem}}) & (x_{\mathrm{cCL/Mem}} < x < x^{\mathrm{MeOH}}_o) \\ N^{\mathrm{O_2}}\big|_{x=x^{\mathrm{MeOH}}_o} - \left[\frac{j^{\mathrm{ORR}} - j^{\mathrm{MOR}}_c}{4F}\right](x - x^{\mathrm{MeOH}}_o) & (x^{\mathrm{MeOH}}_o < x < x_{\mathrm{cCL/cMPL}}) \end{cases}$
cMPL, cBL	$N^{\mathrm{MeOH}}(x) = 0$; $N^{\mathrm{H_2O}}(x) = N^{\mathrm{H_2O}}\big|_{x=x_{\mathrm{cCL/cMPL}}}$; $N^{\mathrm{O_2}}(x) = N^{\mathrm{O_2}}\big|_{x=x_{\mathrm{cCL/cMPL}}}$

tion mechanism of Liu and Wang [12]. More details on the terms given in the cathode flux expressions are given in the later section on the electrochemistry model, but note that the MeOH crossed over into the cCL is explicitly accounted for in the present model.

2.3. Membrane model

The water transport across the membrane is modeled as a result of electro-osmotic drag (EOD), diffusion, and hydraulic-permeation (HP):

$$N^{\mathrm{H_2O}}_{\mathrm{Mem}} = n^{\mathrm{H_2O}}_d\left(\frac{i}{F}\right) + \frac{\rho_{\mathrm{Mem}}}{\mathrm{EW}_{\mathrm{Mem}}} D^{\mathrm{H_2O}}_{\mathrm{Mem}} \frac{\lambda_{\mathrm{aCL}} - \lambda_{\mathrm{cCL}}}{\delta_{\mathrm{Mem}}} + \frac{\rho_l \kappa_{\mathrm{Mem}}}{M_l \mu_l} \frac{p_{l,\mathrm{aCL}} - p_{l,\mathrm{cCL}}}{\delta_{\mathrm{Mem}}} = \alpha \frac{i}{F} \tag{5}$$

The membrane MeOH flux is driven by EOD and diffusion:

$$N^{\mathrm{MeOH}}_{\mathrm{Mem}} = n^{\mathrm{MeOH}}_d\left(\frac{i}{F}\right) + D^{\mathrm{MeOH}}_{\mathrm{Mem}} \frac{c^{\mathrm{MeOH}}_{\mathrm{aCL}} - c^{\mathrm{MeOH}}_{\mathrm{cCL}}}{\delta_{\mathrm{Mem}}} = \frac{i_{\mathrm{xover}}}{6F} \tag{6}$$

Note that all relevant correlations used in these expressions are given in Table 2 along with pertinent references. As alluded to previously, in our model, the aCL and cCL are of finite thickness. Because physically water enters and exits the ionomer phase throughout the thickness of the CLs, we approximate λ and p_l in our algebraic membrane model – Eqs. (5) and (6) – as their average values in the appropriate aCL and cCL. Also, we assume that the EOD coefficients are determined by the water content and MeOH concentration conditions in the aCL (see Table 2).

2.4. Species transport model

In a two-phase region of the anode, we use the Stefan–Maxwell equations for MeOH diffusion in both liquid and vapor phases. With these equations we then solve for the liquid- and vapor-phase superficial MeOH fluxes, sum them, and set the sum equal to the total MeOH species flux, as per Eq. (4). We then assume that local equilibrium exists between MeOH in liquid and vapor phases and apply Henry's law to remove the gas-phase MeOH concentration as a variable. The resulting equation (in 1D), which is solved for the liquid MeOH concentration is given by

$$\frac{c^{\mathrm{MeOH}}_l N^{\mathrm{H_2O}} - c_{t,l} D^{\mathrm{MeOH,H_2O}}_{\mathrm{eff},l} \frac{dc^{\mathrm{MeOH}}_l}{dx}}{c_{t,l} - c^{\mathrm{MeOH}}_l} + \frac{c^{\mathrm{MeOH}}_l N^{\mathrm{CO_2}} - c_{t,g} D^{\mathrm{MeOH,CO_2}}_{g,\mathrm{eff}} (dc^{\mathrm{MeOH}}_l/dx)}{k_H[c^{\mathrm{H_2O}}_{\mathrm{sat}}(D^{\mathrm{MeOH,CO_2}}_g/D^{\mathrm{MeOH,H_2O}}_g) + c^{\mathrm{CO_2}}_g]} = N^{\mathrm{MeOH}}(x) \tag{7}$$

Note here that we use effective diffusivities (modeled with the Bruggeman correlation) and superficial fluxes. With the liquid-phase MeOH concentration known, we solve for the gas-phase MeOH concentration via Henry's law. The total gas-phase concentration is known from the ideal gas law, and the vapor-phase H_2O concentration is known from equilibrium conditions; it follows that the gas-phase CO_2 concentration is calculated from $c^{\mathrm{CO_2}}_g = c_{t,g} - c^{\mathrm{H_2O}}_g - c^{\mathrm{MeOH}}_g$. The total liquid and liquid H_2O concentrations are determined assuming an ideal solution, and from using simple binary solution relationships.

If a single-phase region exists on the anode side of the cell, the MeOH flux is carried entirely by the vapor-phase, and we now must also consider H_2O vapor-phase transport. Utilizing once again the Stefan–Maxwell equations for MeOH and H_2O in the vapor-phase, we get the following equations, which we solve for the vapor-phase MeOH and H_2O concentrations, respectively:

$$\frac{c^{\mathrm{MeOH}}_g N^{\mathrm{CO_2}} + (D^{\mathrm{MeOH,CO_2}}_g/D^{\mathrm{MeOH,H_2O}}_g) c^{\mathrm{MeOH}}_g N^{\mathrm{H_2O}} - c_{t,g} D^{\mathrm{MeOH,CO_2}}_{g,\mathrm{eff}} (dc^{\mathrm{MeOH}}_g/dx)}{c^{\mathrm{H_2O}}_g (D^{\mathrm{MeOH,CO_2}}_g/D^{\mathrm{MeOH,H_2O}}_g) + c^{\mathrm{CO_2}}_g} = N^{\mathrm{MeOH}}(x) \tag{8}$$

$$\frac{c^{\mathrm{H_2O}}_g [N^{\mathrm{CO_2}} + (D^{\mathrm{H_2O,CO_2}}_g/D^{\mathrm{H_2O,MeOH}}_g)] - c_{t,g} D^{\mathrm{H_2O,CO_2}}_{g,\mathrm{eff}} (dc^{\mathrm{H_2O}}_g/dx)}{c^{\mathrm{MeOH}}_g (D^{\mathrm{H_2O,CO_2}}_g/D^{\mathrm{H_2O,MeOH}}_g) + c^{\mathrm{CO_2}}_g} = N^{\mathrm{H_2O}}(x) \tag{9}$$

With the vapor-phase MeOH and H_2O concentrations known, we solve for the gas-phase CO_2 concentration in this single-phase anode region in exactly the same manner as in the two-phase region.

On the cathode side of the cell, we utilize Fick's law to determine the gas-phase O_2 concentration:

$$-D^{\mathrm{O_2}}_{g,\mathrm{eff}} \frac{dc^{\mathrm{O_2}}_g}{dx} = N^{\mathrm{O_2}}(x) \tag{10}$$

Table 2
Relationships and parameters for 1D DMFC model.

Correlation or value	Description	Comment
$k_{rl} = s^4$	Liquid-phase relative permeability.	Ref. [22].
$D_g^{MeOH,H_2O} = D_g^{MeOH,CO_2} = 1.96 \times 10^{-5} \left(\frac{T}{328.15}\right)^{1.823} \frac{1.013 \times 10^5\,Pa}{p}\,m^2/s$	Gas MeOH, H_2O and MeOH, CO_2 diffusivity.	Chapman–Enskog theory for p, T dependence; reference value from [23] for air–MeOH, approximated same for MeOH, H_2O and MeOH, CO_2.
$D_g^{H_2O,CO_2} = 2.01 \times 10^{-5} \left(\frac{T}{307}\right)^{1.823} \frac{1.013 \times 10^5\,Pa}{p}\,m^2/s$	Gas H_2O, CO_2 diffusivity.	Chapman–Enskog theory for p, T dependence; reference diffusivity from [24].
$D_g^{O_2} = 3.57 \times 10^{-5} \left(\frac{T}{352}\right)^{1.823} \frac{1.013 \times 10^5\,Pa}{p}\,m^2/s$	Gas O_2 diffusivity.	Chapman–Enskog theory for p, T dependence; reference diffusivity from [24] for O_2, H_2O.
$D_l^{MeOH,H_2O}(T) = 1.4 \times 10^{-9} \left[\frac{647.3 - 298.15}{647.3 - T}\right]^6 m^2/s$	Liquid MeOH diffusivity.	T dependence from [24]; reference value from [25] for dilute MeOH solution.
$\lambda = \begin{cases} 22 & (s > 0.3) \\ 14 + 8s/0.3 & (s \le 0.3) \\ 0.043 + 17.81RH - 39.85RH^2 + 36.0RH^3 & (\text{vapor}) \end{cases}$	Nafion® membrane water content.	Liquid assumed interpolation, upper and lower values from [26]; vapor from [27].
$D_{Mem}^{MeOH}(T) = 1.5 \times 10^{-10} \exp\left[2416\left(\frac{1}{303} - \frac{1}{T}\right)\right] m^2/s$	Nafion® membrane MeOH diffusivity.	T dependence taken from [27] for H_2O transport in Nafion® with reference value experimentally calibrated at ECEC.
$D_{Mem}^{H_2O}(T) = 4.80 \times 10^{-11} \exp\left[2416\left(\frac{1}{303} - \frac{1}{T}\right)\right] m^2/s$	Nafion® membrane H_2O diffusivity.	T dependence taken from [27] with reference value calibrated at ECEC.
$n_d^{H_2O} = \begin{cases} \left[\frac{\lambda - 14}{8}\right](n_{d,ref}^{H_2O} - 1) + 1 & \text{for } \lambda \ge 14 \\ 1 & \text{for } \lambda < 14 \end{cases}$	H_2O EOD coefficient.	Interpolation assumed; upper and lower values from [3] and [28].
$n_{d,ref}^{H_2O} = 1.6767 + 0.0155(T - 273) + 8.9074 \times 10^{-5}(T - 273)^2$	H_2O reference EOD coefficient for membrane in equilibrium with liquid H_2O.	From Ref. [3].
$n_d^{MeOH} = n_d^{H_2O} \frac{c_l^{MeOH}}{c_{t,l}}$	MeOH drag coefficient.	Assumed similar to Ref. [29].

We take a similar approach to vapor-phase MeOH in the cCL where MeOH is present from membrane crossover. We model the liquid-phase transport again using the Stefan–Maxwell equation, resulting in the following expression which is solved for liquid MeOH concentration.

$$\frac{c_l^{MeOH} N^{H_2O} - c_{t,l} D_{l,eff}^{MeOH,H_2O}(dc_l^{MeOH}/dx)}{c_{t,l} - c_l^{MeOH}} - \frac{D_{g,eff}^{MeOH}}{k_H}\frac{dc_l^{MeOH}}{dx} = N^{MeOH}(x) \tag{11}$$

2.5. Liquid flow model

In the porous media of the fuel cell anode and cathode, there exists liquid flow driven by capillary forces. In this work we follow the theory presented in detail by Pasaogullari and Wang [19,20], and Nam and Kaviany [21], where Darcy's law is used to model the liquid flow through the porous media. In Darcy's law, the liquid flux is proportional to the negative of the gradient in liquid pressure; defining the capillary pressure as $p_c = p_g - p_l$, and noting that we assume the gas phase pressure to be uniform over the porous media, we end up with an expression yielding the liquid flux proportional to the gradient in capillary pressure. Further, using the Leverett function to relate the capillary pressure to the liquid saturation, we end up with the following 1D expression:

$$\frac{\rho_l k_{rl}}{M_l \mu_l}(K\varepsilon)^{1/2}(\sigma\cos\theta)\frac{dJ}{ds}\frac{ds}{dx} = N_l(x) \tag{12}$$

In the 1D model, we solve Eq. (12) for the liquid saturation. Note that wherever liquid MeOH is present, the liquid flux is equal to the sum of the liquid MeOH and H_2O fluxes.

At the interface of two distinct porous layers (e.g. aBL and aMPL), the capillary pressure remains uniform across the interface [20,21]. As a result, a saturation jump model is implemented at those interfaces (given here for two generic adjacent layers A and B):

$$p_{c,A} = p_{c,B} \tag{13a}$$

$$\sigma\cos(\theta_A)\left(\frac{\varepsilon_A}{K_A}\right)^{1/2} J(s_{int,A}) = \sigma\cos(\theta_B)\left(\frac{\varepsilon_B}{K_B}\right)^{1/2} J(s_{int,B}) \tag{13b}$$

2.6. Electrochemistry model

In our model the transport equations are coupled to the cathode electrochemistry model via the flux terms, as given in Table 1. The cathode electrochemistry model is based on the detailed reaction mechanism given by Liu and Wang [12] which accounts for the mixed potential in the cCL caused by the crossed-over MeOH. In order to implement this in the 1D model, we split the cCL into two regions: where MeOH is still present from crossover ($x < x_o^{MeOH}$) and where MeOH is not present ($x > x_o^{MeOH}$). The average volumetric reaction current densities for MOR and ORR, j_c^{MOR}, and j^{ORR}, and the average volumetric chemical reaction rate, r_{chem}, are defined in the region ($x < x_o^{MeOH}$). As part of this model, we calculate η_c, j_c^{MOR}, j^{ORR}, and r_{chem} from the following expressions, with all quantities

defined by their average values in the cCL:

$$\eta_c = \frac{RT}{\alpha_c F} \ln\left(\frac{j^{\mathrm{ORR}}}{j^{\mathrm{ORR}}_{\mathrm{ref}}} \frac{c^{\mathrm{O_2}}_{g,\mathrm{ref}}}{c^{\mathrm{O_2}}_{g}} \frac{1}{1-s}\right) \tag{14}$$

$$j^{\mathrm{MOR}}_c = 6aFKk_4 \exp\left[\frac{(1-\beta_4)FV_c}{RT}\right] \theta^{\mathrm{CO}}\theta^{\mathrm{OH}} \tag{15}$$

$$j^{\mathrm{ORR}} = \frac{i}{\delta_{\mathrm{cCL}}} + j^{\mathrm{MOR}}_c \tag{16}$$

$$r_{\mathrm{chem}} = aK_r[c^{\mathrm{MeOH}}_l]^{\beta}[c^{\mathrm{O_2}}_g]^{\gamma} \tag{17}$$

We take the equations for the CO and OH surface coverages directly from Ref. [12]:

$$\theta_{\mathrm{CO}} = b\frac{k_2 \exp[\alpha_2 FV_c/RT]}{k_4 \exp[(1-\beta_4)FV_c/RT]} \tag{18}$$

$$\theta_{\mathrm{OH}} = \frac{k_1\overline{c^{\mathrm{MeOH}}}(1-\theta_{\mathrm{CO}})}{b\{k'_1 + k_2 \exp[\alpha_2 FV_c/RT] + k_1\overline{c^{\mathrm{MeOH}}}\} + k_1\overline{c^{\mathrm{MeOH}}}} \tag{19}$$

$$b = \frac{k'_3 \exp[-\beta_3 FV_c/RT]}{(\{k'_1 + k_2 \exp[\alpha_2 FV_c/RT]\}k_3 \exp[(1-\beta_3)FV_c/RT])/(k_1\overline{c^{\mathrm{MeOH}}}) + k_2 \exp[\alpha_2 FV_c/RT]} \tag{20}$$

Note that in these expressions, V_c is the average cathode potential in the cCL, which can be expressed as

$$V_c = \eta_c + U^{\mathrm{ORR}}_o \tag{21}$$

As illustrated in Table 1 the species flux terms in the cCL (which are essentially the source terms in the transport equations) are obviously functions of the reaction rates given by Eqs. (15)–(17). The reaction rates given by Eqs. (15)–(17) (and complimentary Eqs. (14) and (18)–(20)) are likewise functions of the cCL species concentrations. Hence, the cathode electrochemistry and transport models are coupled, and must be solved simultaneously. It is worth noting that while our cathode electrochemistry model is based on that of Liu and Wang [12], the way we implement it in our model is somewhat different. The anode electrochemistry and transport models are not coupled because we assume a uniform reaction rate in the aCL and calculate the anode overpotential after the transport problem has been solved. Hence, we end up with i (current density) in the aCL flux terms (see Table 1), which is an input to the model. Because we only present results from the transport model in this work, further details of the anode electrochemistry model are not needed.

2.7. Boundary conditions

The MeOH and O_2 concentration boundary conditions (at the BL/flow channel interface) are estimated based on a simple 1D mass balance analysis of the flow channel:

$$c^{\mathrm{MeOH}}_l\big|_{\substack{\text{anode}\\ \text{boundary}}} = c^{\mathrm{MeOH}}_{l,0}\left[1 - \frac{1}{2\xi_a(i_{\mathrm{ref},a}/i)}\right] \tag{22}$$

$$c^{\mathrm{O_2}}_g\big|_{\substack{\text{cathode}\\ \text{boundary}}} = c^{\mathrm{O_2}}_{g,0}\left[1 - \frac{1}{2\xi_c(i_{\mathrm{ref},c}/i)}\right] \tag{23}$$

The anode and cathode liquid saturation boundary conditions are assumed as

$$s\big|_{\substack{\text{anode}\\ \text{boundary}}} = 0.8 \tag{24}$$

Table 3
Baseline DMFC parameters.

Parameter	Value
δ_{aBL} (μm)	260
δ_{aMPL} (μm)	20
δ_{aCL} (μm)	15
δ_{Mem} (μm)	50
δ_{cCL} (μm)	15
δ_{cMPL} (μm)	20
δ_{cBL} (μm)	260
$\varepsilon_{\mathrm{aBL}}$, $\varepsilon_{\mathrm{cBL}}$	0.6
$\varepsilon_{\mathrm{aMPL}}$, $\varepsilon_{\mathrm{cMPL}}$	0.4
$\varepsilon_{\mathrm{aCL}}$, $\varepsilon_{\mathrm{cCL}}$	0.6
κ_{aBL}, κ_{cBL} (m^2)	1.0×10^{-14}
κ_{aMPL}, κ_{cMPL} (m^2)	2.0×10^{-15}
κ_{aCL}, κ_{cCL} (m^2)	3.6×10^{-16}
κ_{Mem} (m^2)	4.0×10^{-20}
θ_{aBL}, θ_{cBL} (°)	110
θ_{aMPL}, θ_{cMPL} (°)	120
θ_{aCL}, θ_{cCL} (°)	96
T (K)	333
p (Pa)	101,325
$c^{\mathrm{MeOH}}_{l,o}$ (M)	2.0
ξ_a @ $i_{\mathrm{ref}} = 150$ mA cm^{-2}	2.0
ξ_c @ $i_{\mathrm{ref}} = 150$ mA cm^{-2}	2.0

$$s\big|_{\substack{\text{cathode}\\ \text{boundary}}} = \begin{cases} 0.1 & i < 1000\,\mathrm{A/m^2} \\ 0.1\left(\dfrac{i}{1000\,\mathrm{A/m^2}}\right)^{1.5} & i > 1000\,\mathrm{A/m^2}, \\ \text{with maximum of } 0.9 & \end{cases} \tag{25}$$

2.8. Numerical implementation and solution

In the 1D model, the anode and cathode are coupled by the membrane model. Further, due to the detailed cathode mixed potential model, the transport, liquid flow, and cathode electrochemistry models are coupled. In the solution procedure, all differential equations are differenced using a backwards-differencing scheme. Further, we implement an iterative scheme which calculates the required membrane fluxes and coupled reaction rates using a hybrid secant/bi-section method. Based on the iterative values of these parameters, we solve the transport and liquid saturation problem utilizing a Gauss–Seidel iteration method. The entire system is iterated until converged; strict error tolerances are used for each variable individually, and residuals are checked to ensure convergence.

3. Results and discussion

3.1. Hydrophobic anode MPL effect

Table 3 gives the baseline DMFC parameters used in this study. Fig. 3(a) illustrates the net water transport coefficient versus cell current density, and Fig. 3(b) gives the EOD, diffusion, and hydraulic-permeation components of α both for the baseline cell with and without the aMPL. Note that the α components are simply the H_2O membrane flux components given in Eq. (5) times (F/i) (e.g. $\alpha_{\mathrm{EOD}} = n_d^{\mathrm{H_2O}}$). The effectiveness of the hydrophobic aMPL in reducing α is clear from these plots; without the aMPL present, α is ~2.0–2.2, but is reduced to 0.25–0.4 with the aMPL in the operating current density range of 150–200 mA cm^{-2}. Fig. 3(b) clearly shows that the MEA with aMPL has significantly lower EOD and significantly greater back diffusion from cathode to anode. The near-zero value of α_{HP} is in part due to the fact that we are simulating a cell with the same CL and MPL properties on each side of the membrane, thereby making it difficult to generate a large

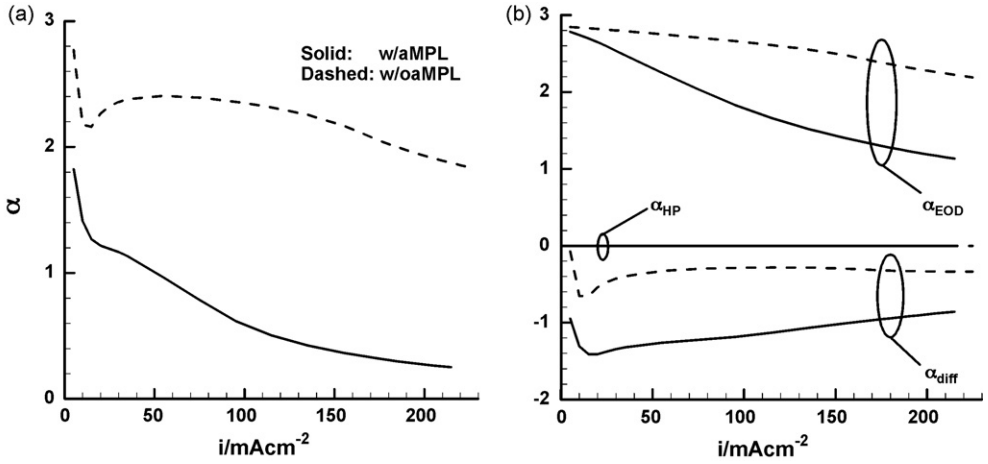

Fig. 3. (a) Net water transport coefficient (α) and (b) electro-osmotic drag (EOD), diffusion (diff), and hydraulic pressure (HP) α components vs. cell current density with and without hydrophobic anode micro-porous layer (aMPL).

gradient of liquid pressure across the membrane. The liquid saturation profiles given in Fig. 4 for various current densities help to explain physically how the hydrophobic aMPL causes this considerable reduction in α. At each of the three current densities, the liquid saturation level is lower in the aCL with the hydrophobic aMPL present. This reduction in aCL saturation acts to both reduce the EOD coefficient and increase the difference in water content across the membrane, thereby increasing back diffusion from cathode to anode.

Note that the lower liquid saturation level in the aCL is caused by the hydrophobic nature of the aMPL in the following manner. The saturation level in the aMPL is far lower than in the aBL due to the saturation jump. At a lower saturation level, the liquid-phase relative permeability is much lower in Darcy's law, Eq. (12) (see Table 2, in this work, we have assumed $k_{rl} = s^4$); this ultimately causes a significantly larger drop in saturation over the aMPL thickness when compared with an equivalent length aBL section. This large drop in liquid saturation over the thickness of the aMPL ultimately leads to

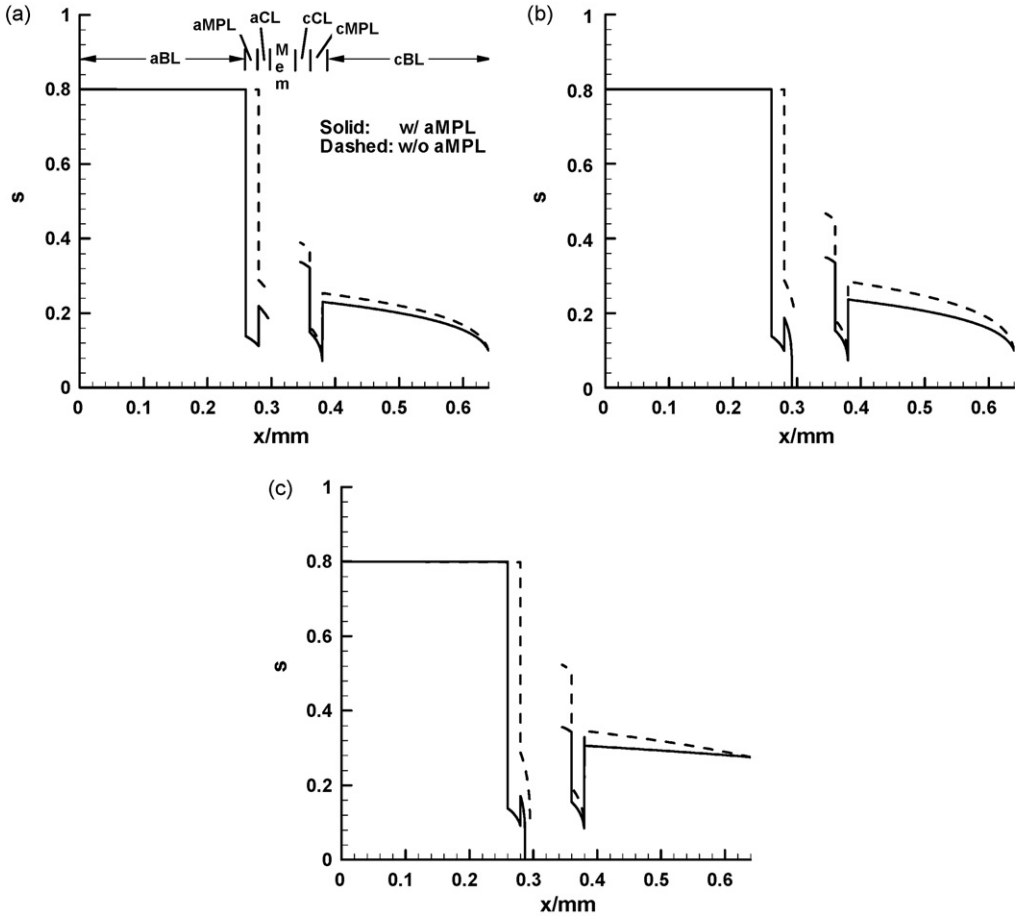

Fig. 4. Saturation profiles with and without hydrophobic anode micro-porous layer (aMPL); (a) $i = 50\,mA\,cm^{-2}$, (b) $i = 100\,mA\,cm^{-2}$, and (c) $i = 150\,mA\,cm^{-2}$.

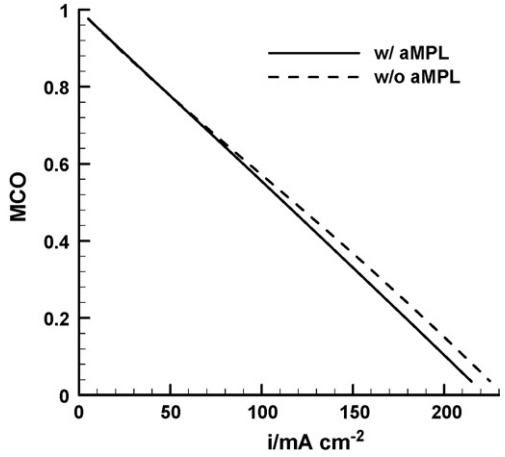

Fig. 5. Methanol crossover ratio (MCO) vs. cell current density with and without anode micro-porous layer (aMPL).

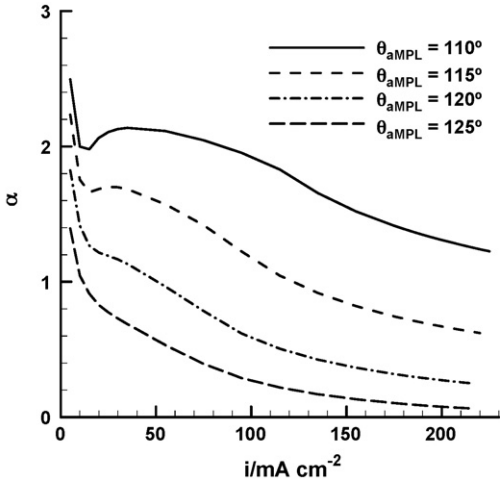

Fig. 7. Net water transport coefficient (α) vs. cell current density for anode micro-porous layer (aMPL) contact angles θ_{aMPL} = 110°, 115°, 120°, and 125°.

a significantly different capillary pressure, p_c, at the aCL interface, as compared with only aBL present. As per Eqs. (13a) and (13b), this different capillary pressure leads to a reduced saturation level in the aCL. It is therefore the saturation jump at the aBL/aMPL interface coupled with the low liquid-phase permeability at low saturation (in the aMPL) that lead to the low aCL saturation, and the reduction in α as described.

From Fig. 5 we see that in addition to reducing the water crossover, a hydrophobic aMPL also slightly reduces the methanol crossover to the cathode. At any given current density, it is evident from Fig. 5 that the MCO is lower with hydrophobic aMPL present, i.e. the fuel efficiency is higher. This is a direct consequence of the dilution effect a lower α has on the methanol concentration in the aCL, as further illustrated by Fig. 6, which shows the methanol and H_2O liquid concentration profiles in the anode with and without hydrophobic aMPL at i = 150 mA cm^{-2}. Here we see that with the hydrophobic aMPL present, the methanol concentration is less than, and the H_2O concentration is greater than without aMPL. From Eq. (6) we see that the EOD and diffusion components of MeOH crossover are both increasing functions of the methanol concentration in the aCL, and hence it is clear that the dilution effect causes a lower MCO.

It is further important to note from Fig. 6 that even though the liquid H_2O concentration profile increases towards the membrane, it does not imply that there is a net flux of H_2O towards the anode flow channel. Indeed, there is a diffusion flux towards the anode flow channel (negative x-direction). However, due to the capillary-induced liquid flow, there is an advection of liquid towards the aCL, and hence net H_2O transport is still towards the aCL (positive x-direction). Obviously, due to the binary nature of the liquid methanol/water mixture, where the concentration of H_2O is greater, the concentration of methanol must necessarily be less.

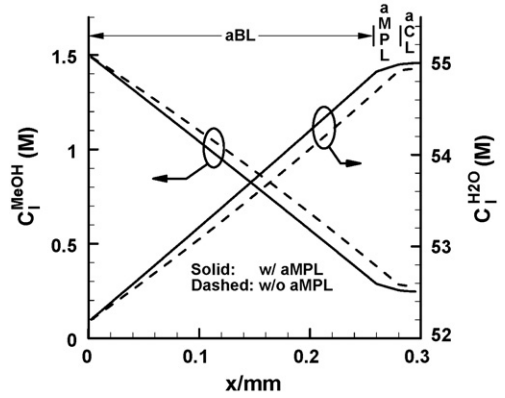

Fig. 6. Liquid CH_3OH and H_2O anode concentration profiles with and without hydrophobic anode micro-porous layer (aMPL) at i = 150 mA cm^{-2}.

3.2. Parametric study—effect of anode MPL properties

3.2.1. Contact angle

Fig. 7 shows the α versus current density curves for a cell with baseline parameters except with varying aMPL contact angle. It is evident that a higher contact angle (i.e. more hydrophobic to methanol–water solutions) yields a lower water crossover, with α ranging from ~1.3–1.6 for θ_{aMPL} = 110° to ~0.1–0.2 for θ_{aMPL} = 125° in the current density range of i = 150–200 mA cm^{-2}. Fig. 8 illustrates that the greater hydrophobicity acts to increase the saturation jump at the aBL/aMPL interface, thereby reducing the saturation level in the aMPL. As described in the previous section, this lower aMPL saturation level ultimately acts to reduce the liquid saturation level in the aCL, thereby reducing α.

It is worth noting in Eq. (12) that a larger contact angle directly acts to reduce the gradient in saturation for a given liquid flux, which would theoretically lead to a higher aCL saturation level.

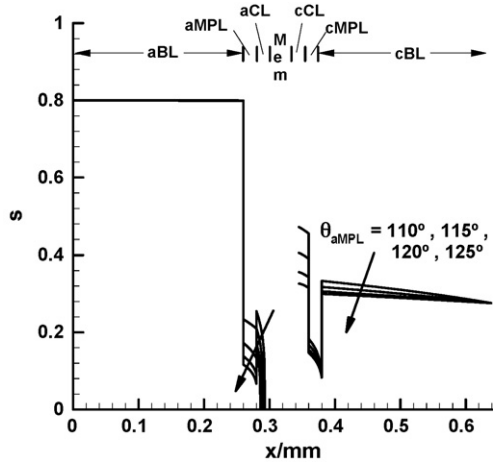

Fig. 8. Liquid saturation profiles for anode micro-porous layer (aMPL) contact angles θ_{aMPL} = 110°, 115°, 120°, and 125°; i = 150 mA cm^{-2}.

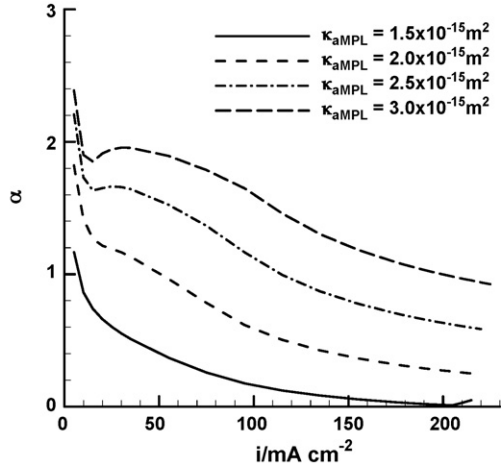

Fig. 9. Net water transport coefficient (α) vs. cell current density for anode micro-porous layer (aMPL) permeabilities $\kappa_{aMPL} = 1.5 \times 10^{-15}$, 2.0×10^{-15}, 2.5×10^{-15}, and 3.0×10^{-15} m^2.

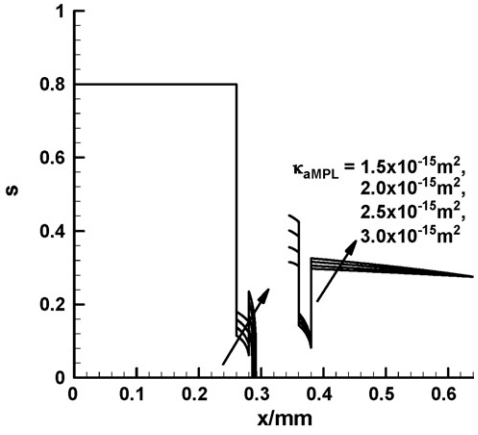

Fig. 10. Liquid saturation profiles for anode micro-porous layer (aMPL) permeabilities $\kappa_{aMPL} = 1.5 \times 10^{-15}$, 2.0×10^{-15}, 2.5×10^{-15}, and 3.0×10^{-15} m^2; $i = 150$ mA cm^{-2}.

However, as evidenced by Figs. 7 and 8, this effect is secondary to the contact angle effect on saturation jump at the aBL/aMPL interface, and the mechanism for lower aCL saturation as described in Section 3.1.

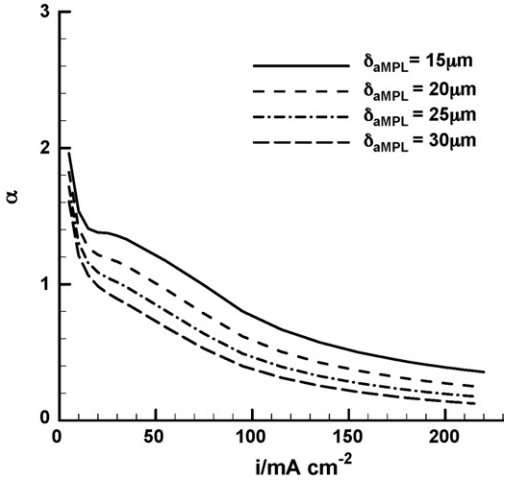

Fig. 11. Net water transport coefficient (α) vs. cell current density for anode micro-porous layer (aMPL) thicknesses $\delta_{aMPL} = 15$, 20, 25, and 30 μm.

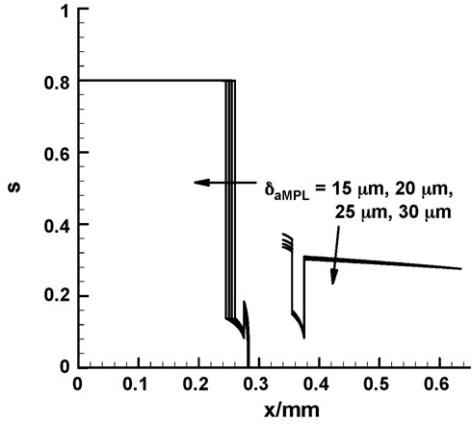

Fig. 12. Liquid saturation profiles for anode micro-porous layer (aMPL) thicknesses $\delta_{aMPL} = 15$, 20, 25, and 30 μm; $i = 150$ mA cm^{-2}; note that curves for 20, 25, and 30 μm aMPLs have been shifted to align to the membrane for all thicknesses.

3.2.2. Permeability

Fig. 9 shows the α versus current density profile for baseline cell parameters, except for variable aMPL permeability. This plot shows that a lower permeability leads to a reduction in α, which is seen to be ~1–1.25 for $\kappa_{aMPL} = 3.0 \times 10^{-15}$ m^2, and 0.025–0.04 for $\kappa_{aMPL} = 1.5 \times 10^{-15}$ m^2 for $i = 150$–200 mA cm^{-2}. Fig. 10 shows that the greatest effect of smaller aMPL permeability is in reducing the saturation level in the aMPL and a corresponding reduction in the aCL. Note from Eq. (12) that a reduced aMPL permeability also acts to increase the saturation gradient in the aMPL, which ultimately reduces the saturation in the aCL. However, once again this effect is secondary to the influence of lower permeability on saturation level in the aMPL via interfacial saturation jump, and hence lower liquid-phase relative permeability.

3.2.3. Thickness

Finally, Figs. 11 and 12 show the α versus current density and saturation profile plots for MEAs with baseline parameters, but with different aMPL thicknesses. From Fig. 11 we see that a thicker aMPL acts to reduce α, being ~0.4–0.52 for aMPL thickness of 15 μm, and ~0.12–0.2 for aMPL thickness of 30 μm, again for $i = 150$–200 mA cm^{-2}. As shown in Fig. 12, the aMPL thickness obviously does not affect the saturation jump at the aBL/aMPL interface, but it does reduce the saturation level in the aCL simply due to the fact that it creates a longer distance over which the liquid must be transported.

4. Conclusions

We have used a 1D, two-phase transport model that accounts for capillary-induced liquid flow in porous media to study the water transport characteristics of a Nafion® 112-based low-α MEA for DMFCs. Specifically, we have physically described how a hydrophobic aMPL acts to reduce the water crossover to the cathode. Our model shows that this is accomplished primarily by lower electro-osmotic drag and enhanced back diffusion, both due to lower liquid saturation in the aCL. Further, it is shown that via dilution of methanol in the aCL, the lower α caused by hydrophobic aMPL reduces the MCO (i.e. increases the fuel efficiency). Finally, a detailed parametric study has demonstrated that an aMPL with higher hydrophobicity, lower permeability, and greater thickness acts to reduce the amount of water crossover to the cathode. The lowered water crossover will in turn enable the direct use of higher concentration methanol fuel in the DMFC anode, as demonstrated in Refs. [7,15].

Acknowledgement

Financial support of this work by ECEC industrial sponsors is gratefully acknowledged.

Appendix A. Nomenclature

a	specific reaction area
α	net water transport coefficient
α_c	ORR cathodic charge transfer coefficient
β	kinetic parameter for chemical reaction
β_4	kinetic rate parameter for MOR
c_q^{ψ}	molar concentration of species ψ in phase q
$c_{q,o}^{\psi}$	molar concentration of species ψ in phase q at inlet of flow channel
$c_{\text{sat}}^{\text{H}_2\text{O}}$	saturated gas-phase molar concentration of H_2O
$c_{t,q}$	total molar concentration of phase q
δ	thickness
$D_q^{\psi_1\psi_2}$	diffusivity of species ψ_1 and ψ_2 in phase q
D_{Mem}^{ψ}	diffusivity for species ψ in the membrane
EW	equivalent weight
ε	porosity
F	Faraday's constant
γ	kinetic parameter for chemical reaction
η	efficiency; overpotential
i	current density
j^{ORR}	volumetric ORR rate in cathode catalyst layer
j_c^{MOR}	volumetric MOR rate in cathode catalyst layer
J	Leverett function
k_H	Henry constant
k_{rl}	liquid-phase relative permeability
k_4	kinetic rate parameter for MOR
K	rate coefficient for MOR
K_r	chemical reaction rate coefficient
κ	permeability
λ	water content
M	molecular weight
μ	viscosity
n_d^{ψ}	electro-osmotic drag coefficient for species ψ
N^{ψ}	superficial flux of species ψ in all phases
N_q^{ψ}	superficial flux of species ψ in phases q
N_{Mem}^{ψ}	superficial flux of species ψ across the membrane
p	pressure
θ	contact angle; surface coverage
r_{chem}	volumetric chemical reaction rate in cathode CL
R	universal gas constant
ρ	density
s	liquid saturation (i.e. volume fraction of liquid in the pore space)
σ	surface tension
T	temperature
U_o^{ORR}	equilibrium potential of oxygen reduction reaction
V_c	cathode potential
x	coordinate

Subscripts

a	anode
c	cathode; capillary
diff	diffusion
eff	effective
fuel	fuel
g	gas
HP	hydraulic pressure
l	liquid
Mem	membrane
ref	reference
t	total
xover	crossover

Superscript

ψ	generic species

References

[1] C.K. Dyer, J. Power Sources 106 (2002) 31.
[2] C.Y. Wang, Chem. Rev. 104 (2004) 4727.
[3] G. Lu, C.Y. Wang, in: B. Sunden, M. Faghri (Eds.), Transport Phenomena in Fuel Cells (Developments in Heat Transfer), vol. 19, WIT Press, Boston, 2004 (Chapter 9).
[4] S.K. Kamarudin, W.R.W. Daud, S.L. Ho, U.A. Hasran, J. Power Sources 163 (2007) 743.
[5] G.Q. Lu, F.Q. Liu, C.Y. Wang, Electrochem. Solid-State Lett. 8 (2005) A1.
[6] F. Liu, G. Lu, C.Y. Wang, J. Electrochem. Soc. 153 (2006) A543.
[7] C.Y. Wang, F. Liu, Proceedings of the 8th Small Fuel Cell Symposium, Washington, DC, April, 2006 (Chapter 10).
[8] A. Blum, T. Duvdevani, M. Philosoph, N. Rudoy, E. Peled, J. Power Sources 117 (2003) 22.
[9] C. Lim, C.Y. Wang, J. Power Sources 113 (2003) 145.
[10] K.Y. Song, H.K. Lee, H.T. Kim, J. Electrochim. Acta 53 (2007) 637.
[11] J.Y. Park, J.H. Lee, S.K. Kang, J.H. Sauk, I. Song, J. Power Sources 178 (2008) 181.
[12] F. Liu, C.Y. Wang, J. Electrochem. Soc. 154 (2007) B514.
[13] X. Ren, F.W. Kovacs, K.J. Shufon, S. Gottesfeld, US Patent Pub. No. US 2004/0209154 A1 (2004).
[14] C.Y. Wang, G. Lu, W. Liu, F. Liu, Y. Sato, E. Sakaue, K Matsuoka, US Patent Pub. No. US 2006/0134487 A1 (2006).
[15] C.Y. Wang, F. Liu, Y. Sato, E. Sakaue, US Patent Pub. No. US 2007/0087234 A1 (2007).
[16] F.Q. Liu, Ph.D. Thesis, The Pennsylvania State University, University Park, Pennsylvania, 2006.
[17] F.Q. Liu, C.Y. Wang, Electrochim. Acta 53 (2008) 5517.
[18] W. Liu, Ph.D. Thesis, The Pennsylvania State University, University Park, Pennsylvania, 2005.
[19] U. Pasaogullari, C.Y. Wang, J. Electrochem. Soc. 151 (2004) A399.
[20] U. Pasaogullari, C.Y. Wang, Electrochim. Acta 49 (2004) 4359.
[21] J.H. Nam, M. Kaviany, Int. J. Heat Mass Transfer 46 (2003) 4595.
[22] R.H. Brooks, A.T. Corey, Hydrology Papers, vol. 3, Colorado State University, 1964.
[23] R.B. Mrazek, C.E. Wicks, K.N.S. Prabhu, J. Chem. Eng. Data 13 (1968) 508.
[24] B.E. Poling, J.M. Prausnitz, J.P. O'Connell, The Properties of Gases and Liquids, 5th ed., McGraw-Hill, New York, 2001.
[25] Z.J. Derlacki, A.J. Easteal, V.J. Edge, L.A. Woolf, Z. Roksandic, J. Phys. Chem. 89 (1985) 5318.
[26] T.A. Zawodzinski, C. Derouin, S. Radzinski, R.J. Sherman, V.T. Smith, T.E. Springer, S. Gottesfeld, J. Electrochem. Soc. 140 (1993) 1041.
[27] T.E. Springer, T.A. Zawodzinski, S. Gottesfeld, J. Electrochem. Soc. 138 (1991) 2334.
[28] T.A. Zawodzinski, J. Davey, J. Valerio, S. Gottesfeld, Electrochim. Acta 40 (1995) 297.
[29] W. Liu, C.Y. Wang, J. Electrochem. Soc. 154 (2007) B352.